© 2021. Published by The Company of Biologists Ltd | Journal of Cell Science (2021) 134, jcs256156. doi:10.1242/jcs.256156

RESEARCH ARTICLE

A lamin A/C variant causing striated muscle disease provides insights into filament organization

Rafael Kronenberg-Tenga[1,*], Meltem Tatli[1,*], Matthias Eibauer[1], Wei Wu[2], Ji-Yeon Shin[2], Gisèle Bonne[3], Howard J. Worman[2] and Ohad Medalia[1,‡]

ABSTRACT

The *LMNA* gene encodes the A-type lamins, which polymerize into ∼3.5-nm-thick filaments and, together with B-type lamins and associated proteins, form the nuclear lamina. Mutations in *LMNA* cause a wide variety of pathologies. In this study, we analyzed the nuclear lamina of embryonic fibroblasts from *Lmna*$^{H222P/H222P}$ mice, which develop cardiomyopathy and muscular dystrophy. Although the organization of the lamina appeared unaltered, there were changes in chromatin and B-type lamin expression. An increase in nuclear size and consequently a relative reduction in heterochromatin near the lamina allowed for a higher resolution structural analysis of lamin filaments using cryo-electron tomography. This was most apparent when visualizing lamin filaments *in situ* and using a nuclear extraction protocol. Averaging of individual segments of filaments in *Lmna*$^{H222P/H222P}$ mouse fibroblasts resolved two polymers that constitute the mature filaments. Our findings provide better views of the organization of lamin filaments and the effect of a striated muscle disease-causing mutation on nuclear structure.

KEY WORDS: Cryo-electron tomography, Intermediate filaments, Lamins

INTRODUCTION

Nuclear lamins are the intermediate filament (IF) building blocks of the nuclear lamina on the nucleoplasmic aspect of the inner nuclear membrane of metazoan cells (Fisher et al., 1986; McKeon et al., 1986). They are classified as type V IF proteins based on their sequences (Steinert and Roop, 1988). Similar to cytoplasmic IF proteins, lamins contain a long rod domain comprised of four coiled-coil α-helical segments, termed 1A, 1B, 2A and 2B, separated by flexible linkers (Gruenbaum and Foisner, 2015). This domain is flanked by a non-helical N-terminal head and C-terminal tail domains. The C-terminal domain has a nuclear localization sequence and an immunoglobulin (Ig)-like fold.

The nuclear lamina primarily provides mechanical support to the cell nucleus (Maurer and Lammerding, 2019; Pfeifer et al., 2019; Sapra et al., 2020). Four main lamin isoforms are found in mammals. In humans, they are encoded by the *LMNA*, *LMNB1*, *LMNB2* genes, which in somatic cells encode lamin A/C, lamin B1 and lamin B2, respectively (Worman, 2012). Whereas the B-type lamins are expressed in almost all mammalian cell types, the expression of A-type lamins is developmentally regulated and occurs primarily in differentiated cells (Constantinescu et al., 2006; Kim et al., 2011). Both types of lamins are localized to the nuclear periphery; however, small amounts of A-type lamins are also found in the nucleoplasm where they may function in chromatin organization and gene regulation (Naetar et al., 2017).

In solution, lamin dimers form a parallel coiled-coil structure between two monomers (Klapper et al., 1997). These further assemble by head-to-tail association into long polymers, which associate laterally into the mature filaments (de Leeuw et al., 2018; Stuurman et al., 1998). However, due to the flexibility and length of the coiled-coil domain, which is ∼50 nm, structural determination of lamin dimers has been a challenging task (Makarov et al., 2019; Zwerger and Medalia, 2013). A detailed atomic model of full-length lamin proteins is still elusive. However, structures of lamin A fragments (Ahn et al., 2019; Herrmann and Aebi, 2004; Kapinos et al., 2011; Lilina et al., 2019) have exemplified the interactions between lamin coil 1B to form a tetrameric filament (Ahn et al., 2019; Lilina et al., 2019). The atomic structure of the Ig-like fold of human lamin A/C has also been determined, exhibiting a globular two β-sheets structure (Dhe-Paganon et al., 2002; Krimm et al., 2002). The analysis of coiled-coil fragments has provided insights into the intra-organization of lamin dimers (Strelkov et al., 2004). Based on such analysis (Ahn et al., 2019), an alternative model for lamin assembly has been proposed in which lateral interactions between the coiled-coil domains of the dimers govern the lateral assembly, thus avoiding formation of a head-to-tail polymer. An analysis of lamin filaments in fibroblasts has shown that lamins assemble into 3.5-nm-thick filaments within a ∼14-nm-thick meshwork attached to the inner nuclear membrane (Turgay et al., 2017). The filaments exhibit a short persistence length of <200 nm, which not only hints at their unique mechanical properties and flexibility (Sapra et al., 2020), but also imposes a major challenge for structural reconstruction of lamin filaments.

Mutations in the genes encoding lamins, particularly *LMNA*, cause human diseases termed laminopathies (Tatli and Medalia, 2018; Worman and Bonne, 2007). The most common of these rare laminopathies is dilated cardiomyopathy usually associated with muscular dystrophy (Maggi et al., 2016; Nicolas et al., 2019). The *LMNA* p.His222Pro (hereafter H222P) missense mutation was first identified in a family with autosomal dominant Emery–Dreifuss muscular dystrophy (Bonne et al., 2000). Homozygous *Lmna*$^{H222P/H222P}$ mice develop dilated cardiomyopathy and regional skeletal muscular dystrophy that phenocopies the human disease (Arimura et al., 2005; Muchir et al., 2012). Cells from *Lmna*$^{H222P/H222P}$ mice have altered stiffness (Chatzifrangkeskou

[1]Department of Biochemistry, University of Zurich, Winterthurerstrasse 190, 8057 Zurich, Switzerland. [2]Department of Medicine and Department of Pathology and Cell Biology, Vagelos College of Physicians and Surgeons, Columbia University, New York, NY 10032, USA. [3]Sorbonne Université, INSERM, Centre de Recherche en Myologie, Institut de Myologie, F-75651 Paris CEDEX 13, France.
*These authors contributed equally to this work

‡Author for correspondence (omedalia@bioc.uzh.ch)

M.E., 0000-0003-0638-9347; G.B., 0000-0002-2516-3258; O.M., 0000-0003-0994-2937

Handling Editor: Kathleen Green
Received 20 October 2020; Accepted 26 January 2021

Journal of Cell Science (2021) 134, jcs256156. doi:10.1242/jcs.256156

et al., 2020) and abnormalities in several cell signaling pathways (Choi et al., 2018). However, it is not clear how this mutation affects the structure of the nuclear lamina and lamin filaments. The H222P amino acid substitution is localized to the linker domain of lamin A/C, between coil 1B and 2A of the proteins. While substitution with a proline would presumably disrupt α-helix structure, it does not play a role in the predicted coiled-coil interactions.

To obtain insights into how the H222P amino acid substitution affects lamin structure, we used several modalities to analyze fibroblasts from *Lmna*$^{H222P/H222P}$ mice. Quantitative immunofluorescence and total internal reflection fluorescence (TIRF) microscopy indicated nuclear alterations in these cells, while cryo-electron tomography (cryo-ET) provided new structural insights into the nuclear lamina and the lamin filaments *in situ* and in ghost nuclei. We show that the nuclear area is increased, whereas heterochromatin is proportionally reduced. This results in an increase in contrast for lamin filaments observed using cryo-ET. Applying averaging approaches to *in silico* fragmented filaments (Martins et al., 2021) produced an unprecedented view of the lamin filaments and their substructures. Moreover, mapping back the structural class averages into their original position on lamin filaments provided better resolved insight into lamin filament organization. Although the structure of lamin is presumably unaffected by the pathogenic H222P amino acid substitution in lamin A/C, the chromatin organization at the nuclear lamina and overall nuclear organization is altered.

RESULTS

The nucleus, lamins and condensed chromatin in *Lmna*$^{H222P/H222P}$ fibroblasts

At a cellular level, the impact of amino acid substitutions in A-type lamins on nuclear organization has been previously demonstrated for several point mutations (Bertrand et al., 2020; Goldman et al., 2004; Scaffidi and Misteli, 2008; Vigouroux et al., 2001). To gain insights into the impact of the lamin A/C H222P amino acid substitution on the nucleus, and in particular on nuclear lamin filaments, we examined immortalized *Lmna*$^{H222P/H222P}$ and wild-type mouse embryonic fibroblasts (MEFs). Using TIRF microscopic analysis, we confirmed that both lamin A/C and lamin B1 were properly localized to the nuclear lamina in *Lmna*$^{H222P/H222P}$ MEFs similar to their localization in wild-type MEFs, but the nuclei appeared larger (Fig. 1A). Quantitative analysis showed that the nuclear area of *Lmna*$^{H222P/H222P}$ MEFs was significantly increased, at 1.09 times the area of wild-type nuclei (Fig. 1B; Fig. S1A), corresponding to increase in nuclear volume and envelope surface (Fig. S1B). We used immunofluorescence microscopy to obtain signals to quantify the amounts of histone H3 lysine 9 trimethylation (H3K9me3, a marker of heterochromatin), histone H3 lysine 27 acetylation (H3K27ac, a marker of transcriptional activity), lamin B1 and lamin A/C in wild-type and *Lmna*$^{H222P/H222P}$ MEFs. This analysis showed that the *Lmna*$^{H222P/H222P}$ MEFs had significantly decreased histone H3K9me3, increased histone H3K27ac, increased lamin B1 and decreased lamin A/C (Fig. 1B,C). When analyzed by immunoblotting, lamin B1 and lamin B2 expression was found to be increased in the *Lmna*$^{H222P/H222P}$ MEFs; however, the histone H3K9me3 signal was slightly increased and the lamin A/C signal was not reduced (Fig. S1C,D). These results suggest that incorporation of lamins into the nuclear lamina is not directly affected by the lamin A/C H222P amino acid substitution in linker 1-2, between coil 1 and 2. The increase in nuclear surface area likely resulted in reduction of heterochromatin levels per nuclear envelope area, rather than changes in the absolute quantity of heterochromatin. The changes in lamin expression are presumably attributed to the increased surface of the nuclear envelope that may induce an upregulation of lamin B1, while the overall chromatin and lamin A/C levels resemble their original amounts.

Nuclear lamina structure in *Lmna*$^{H222P/H222P}$ MEFs

The molecular organization of the nuclear envelope can be visualized using cryo-ET (Harapin et al., 2015; Weber et al., 2019). We cultured cells on an electron microscopy (EM) grid prior to vitrification and focused ion beam (FIB) milling in conjunction with cryo-ET (Rigort et al., 2012). This allowed us to visualize the organization of the nuclear envelope in *Lmna*$^{H222P/H222P}$ MEFs *in situ*. The nuclear membranes, lamin filaments and chromatin were all seen without any apparent structural alterations; however, the lamins were better resolved in the mutant cells (Fig. 2A,B; Fig. S2). Surface rendering of the thin reconstructed sections provided a view of the nuclear envelope regions, including the adjacent cytoplasmic structures (Fig. 2C). The nuclear areas hosting lamin filament meshworks were clearly visible with less chromatin and other nuclear components shadowing the lamins in *Lmna*$^{H222P/H222P}$ MEFs compared to those in wild-type MEFs (Fig. 2C; Fig. S3A,B). The reduced density of nuclear structures at the lamina detected in cryo-tomograms of *Lmna*$^{H222P/H222P}$ nuclear envelopes confirmed the results of the fluorescence microscopy analysis and indicated a reduced interaction of lamins with dense chromatin.

To further enhance visualization of the nuclear lamins, we knocked down vimentin expression and removed the cytoplasm, using short exposure to mild detergent followed by nuclease treatment prior to rapid vitrification (Turgay and Medalia, 2017). This produces ghost nuclei in which lamin filaments can be readily identified and followed over longer distances and throughout large datasets acquired from most positions along the nuclear envelope (Tenga and Medalia, 2020). Here, we applied this procedure and detected lamin filaments in both *Lmna*$^{H222P/H222P}$ and wild-type ghost nuclei (Fig. 3A,B, respectively). The lamin meshworks were better identified in the ghost nuclei from the mutant cells (Fig. 3A,B). A surface rendering of *Lmna*$^{H222P/H222P}$ MEFs showed lamin filaments, nuclear pore complexes and cytoplasmic vimentin filaments (Fig. 3C) that were similar to those previously reported in wild-type fibroblasts (Turgay et al., 2017). The overall organization of lamin filaments in ghost nuclei from *Lmna*$^{H222P/H222P}$ MEFs resembled the wild-type nuclear lamina, as seen by the rendered view of two tomograms (Fig. S3C,D). Whereas nuclease treatment only removed part of the heterochromatin from ghost nuclei of wild-type MEFs, these densities were hardly detected in the ghost nuclei prepared from the *Lmna*$^{H222P/H222P}$ MEFs (Fig. S3C,D, green). Although lamin A/C levels were slightly reduced, immunogold labeling confirmed that a substantial amount of lamin A/C was retained in the nuclear lamina of *Lmna*$^{H222P/H222P}$ ghost nuclei and therefore contributed to the structural analysis presented here (Fig. S4). These experiments and cryo-ET analysis suggest that the overall organization of the nuclear lamins is not substantially altered in *Lmna*$^{H222P/H222P}$ MEFs. Rather, the H222P amino acid substitution in lamin A/C influences the size of the nucleus and the chromatin organization at the interface of the lamina, providing a better view of the nuclear lamina.

Structural organization of lamin filaments by averaging and filament reconstitutions

Lamins dimerize in solutions and form head-to-tail polymers (Stuurman et al., 1998); however, how these long coiled-coils protein structures are further assembled into the filaments of the nuclear lamina remains unknown. The higher contrast of individual

Journal of Cell Science (2021) 134, jcs256156. doi:10.1242/jcs.256156

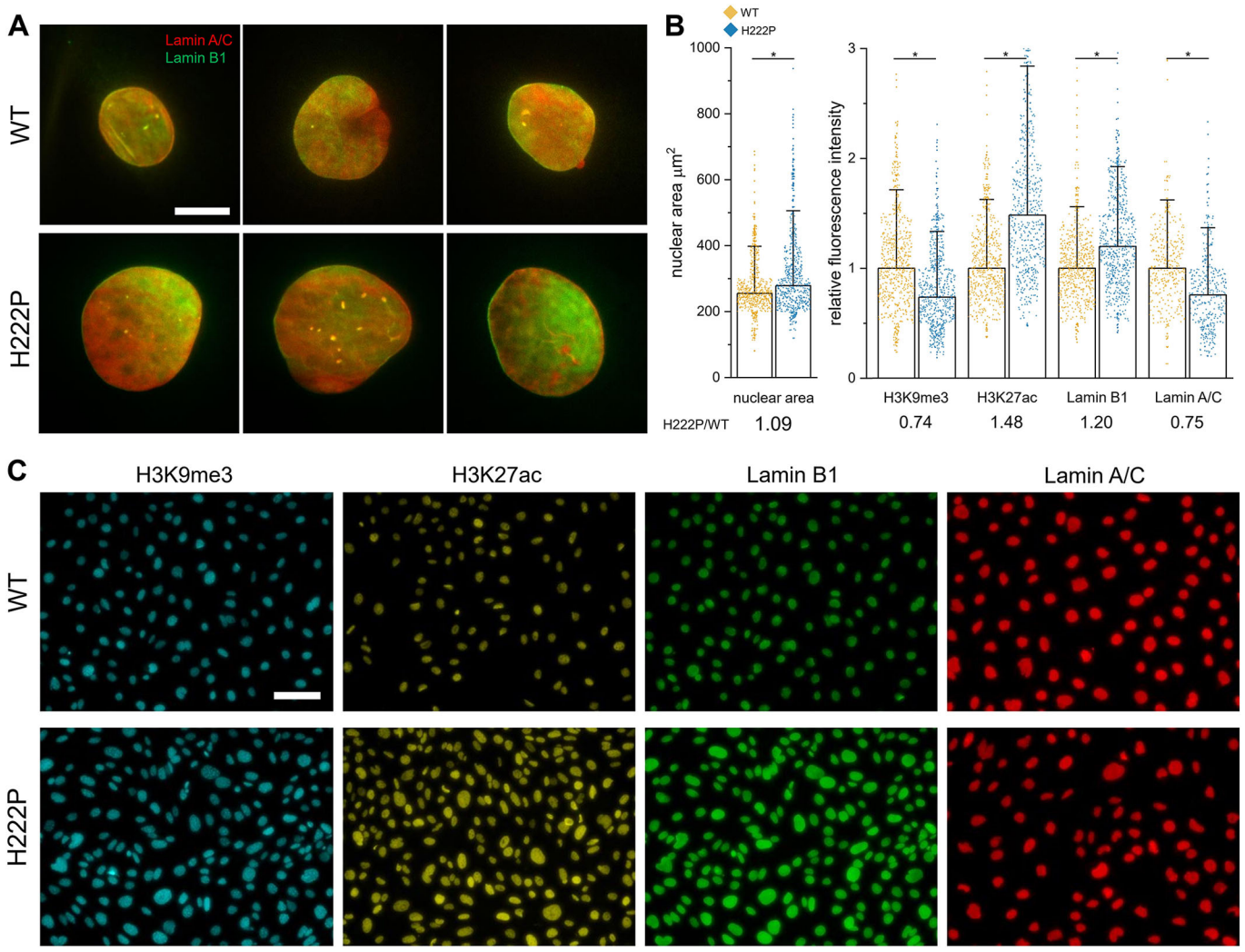

Fig. 1. Nuclear organization of *Lmna*$^{H222P/H222P}$ MEFs. (A) TIRF microscopy images indicate the localization of lamin A/C and lamin B1 in wild-type (WT) and *Lmna*$^{H222P/H222P}$ (H222P) MEFs. Scale bar: 10 µm. (B) Nuclear area and immunofluorescence microscopy-based quantification of histone H3K9me3, histone H3K27ac, lamin B1 and lamin A/C in wild-type and *Lmna*$^{H222P/H222P}$ MEFs. Each dot represents the average signal intensity of a single nucleus. The height of the bars is set to the median and the error bar indicates 1.5 standard deviations. The ratio of median values is shown beneath each graph. Number of nuclei analyzed: nuclear area *n*=602, H3K9me3 *n*=602, H3K27ac *n*=552, lamin B1 *n*=602, lamin A/C *n*=356. **P*<0.05 (one-way ANOVA Tukey's multiple comparison test). (C) Fluorescence microscopy images representative of those used for the quantification in B. Scale bar: 100 µm.

lamin filaments observed by cryo-ET of *Lmna*$^{H222P/H222P}$ MEFs encouraged us to acquire 250 cryo-tomograms of ghost nuclei to gain further insights into their organization and formation. Lamin filaments in these nuclei appeared flexible and often curved, although some filaments exhibited a straight appearance, and were occasionally decorated with globular densities (Fig. 4A). These filaments closely resembled lamin filaments extracted from wild-type MEF ghost nuclei (Fig. S5A). The globular densities were presumably the Ig-like fold domains (Turgay et al., 2017). The position of these globular structures along the filament was roughly regular with some variable distance from the axis of the filaments. This was likely due to the 70-amino-acid linker between the end of helix 2B and the Ig-like fold domain. The heterogeneity in the position of Ig-like fold domains and the heterogeneity of lamin filaments, as well as the possibility of other proteins binding to the lamins, prevented use of conventional averaging approaches to analyze their structure. In order to reduce the complexity and flexibility of these filaments, we therefore fragmented them into short segments (12 nm in length and 4.4 nm in width) *in silico* and calculated their 2D projections followed by a single-particle classification approach (Martins et al., 2021). The restricted width of the analyzed areas allowed us to primarily focus on the coiled-coil rod domains that constructed the core of the filaments, with the risk of partial exclusion of the Ig-like fold domains. Analysis of the prominent 2D classes representing different views revealed substructures within the ∼3.5-nm-diameter lamin filaments, most pronounced among them two ∼1.8-nm-thick filamentous substructures that often interacted and crossed each other, sometimes merging into one structure (Fig. 4B, asterisks; Fig. S5B). We next mapped back the class-averaged structures of lamin filaments to their original coordinates in the ghost nuclei. This produced a set of reconstituted lamin filaments resolved to higher resolution and with higher contrast (Fig. 4C). Two protofilaments composed the mature filaments, interacting with each other and crossing each other frequently but not in a uniform manner (Fig. 4C, asterisks). These substructures resembled in shape and dimensions the head-to-tail polymer of dimers. The presence of two polymer structures within lamin filaments and their heterogenous appearance

Journal of Cell Science (2021) 134, jcs256156. doi:10.1242/jcs.256156

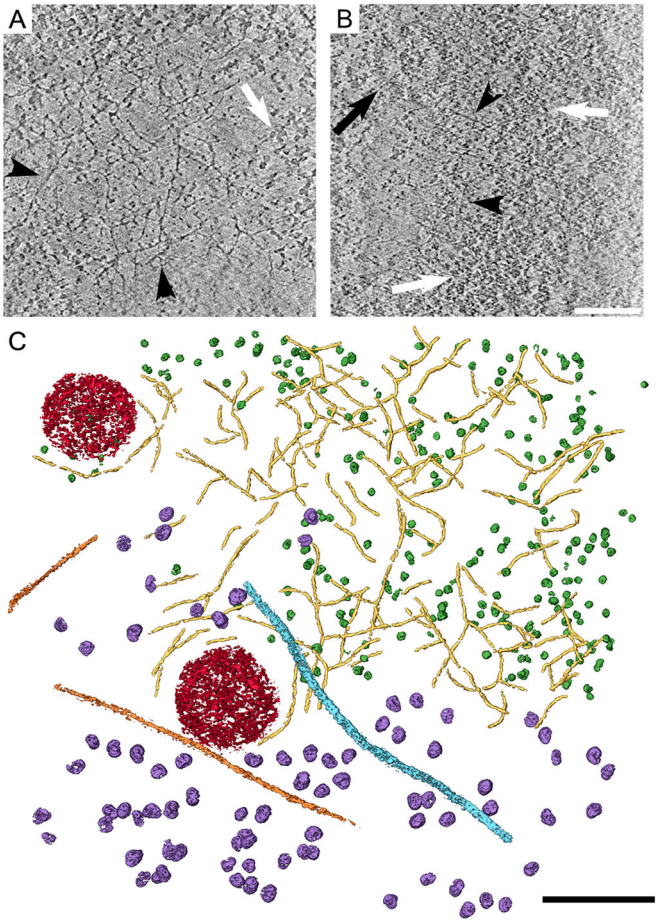

Fig. 2. Visualizing the nuclear lamina in *Lmna*$^{H222P/H222P}$ MEFs, *in situ*. (A, B) Lamin filaments (arrowheads) in an *x*–*y* section, 7 nm in thickness, through a tomogram of *Lmna*$^{H222P/H222P}$ (A) and wild-type (B) MEFs (*n*=45). Lamin filaments are better resolved in the *Lmna*$^{H222P/H222P}$ MEFs. Fewer nucleosomes (white arrows) are in close proximity to the lamina, allowing higher-contrast visualization of lamin filaments (see Fig. S3). Vitrified cells were subjected to cryo-FIB milling prior to cryo-ET (see Materials and Methods). Black arrow indicates a nuclear pore complex. Scale bar: 100 nm. (C) A surface rendering view of the *Lmna*$^{H222P/H222P}$ MEF lamellae shown in A, 150 nm in thickness, shows the organization of lamin filaments (yellow), nucleosomes (green), nuclear pore complexes (red), actin (orange), cytoplasmic vimentin filaments (turquoise) and ribosomes (purple). Scale bar: 100 nm.

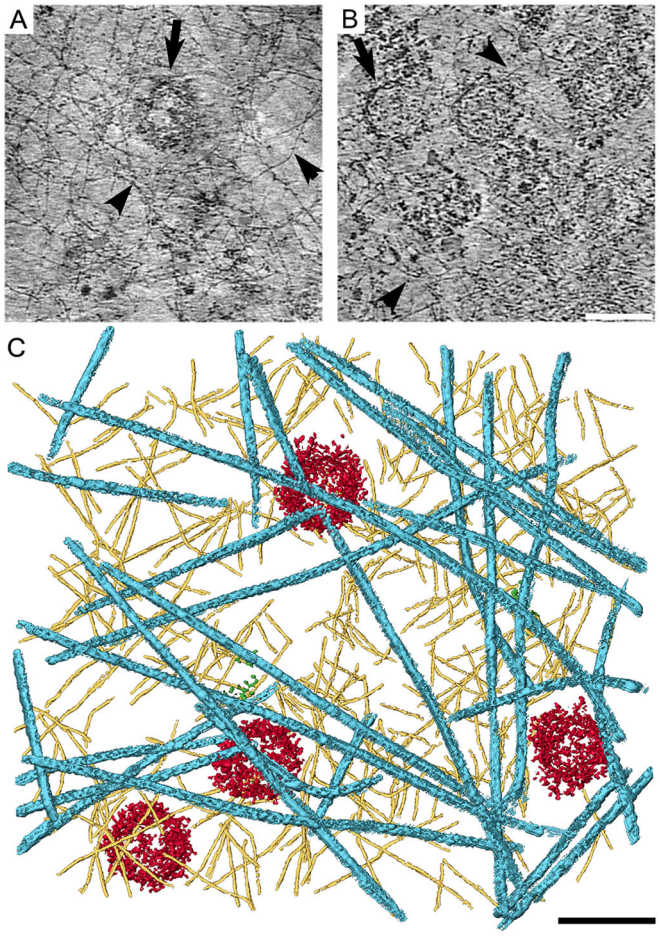

Fig. 3. Visualizing the nuclear lamina in *Lmna*$^{H222P/H222P}$ ghost nuclei resolves the nuclear lamina meshwork. (A,B) Lamin filaments (arrowheads) in an *x*–*y* section, 7 nm in thickness, through tomograms of *Lmna*$^{H222P/H222P}$ (A) and wild-type (B) MEFs. Vitrified ghost nuclei were analyzed by cryo-ET (see Materials and Methods; *n*=233). Black arrows indicate nuclear pore complexes. Scale bar: 100 nm. (C) A surface rendering view of an *Lmna*$^{H222P/H222P}$ MEF ghost nucleus preparation shows the organization of lamin filaments (yellow), nuclear pore complexes (red) and cytoplasmic vimentin filaments (turquoise). Scale bar: 100 nm.

may increase the spectrum of conformations that can be adopted by the mature filaments. This emphasizes the possible variations within the structure. The interactions between the two head-to-tail polymers are varied, allowing tight interactions as well as interactions with a looser appearance, providing additional capability for lamin filaments to fulfill various functions. Resolving the 3D structure of the lamin filaments, together with their Ig-like fold domains, could provide additional information on lamin assembly and the differences between A- and B-type lamin filaments. However, a larger dataset would be needed in addition to an innovative image processing approach.

DISCUSSION

Based on our data, we have generated a model of the nuclear envelope and lamin organization in wild-type and *Lmna*$^{H222P/H222P}$ MEFs (Fig. 5). Nuclei of *Lmna*$^{H222P/H222P}$ MEFs had a larger 2D surface area and less densely-packed heterochromatin and likely chromatin-associated factors. Although the lamin filaments of the lamina of *Lmna*$^{H222P/H222P}$ MEFs were structurally similar to wild-type lamin filaments, they were better visualized by cryo-ET, presumably because of decreased interactions with the densely-packed chromatin at the nuclear periphery. Vimentin knockdown reduced the density of cytoplasmic filaments around nuclei. Although it may alter the forces exerted onto the nuclear lamina, knockdown of vimentin is unlikely to alter the structure of individual lamin filaments. Previous super-resolution microscopy analysis has indicated that the lamina organization in wild-type and vimentin-knockout MEFs is indistinguishable (Turgay et al., 2017). Therefore, reduction in vimentin levels should have limited effects on nuclear lamina organization.

The contrast of the lamin filaments in nuclei of *Lmna*$^{H222P/H222P}$ MEFs was substantially higher than that of the filaments previously observed in MEFs with wild-type *Lmna* (Turgay et al., 2017). This provides us with a unique system to obtain a better resolved view of lamin filaments. Our results suggest that the distribution of lamin filaments within the lamina of the *Lmna*$^{H222P/H222P}$ MEFs is presumably unaffected. The lamina of most somatic cells is

Journal of Cell Science (2021) 134, jcs256156. doi:10.1242/jcs.256156

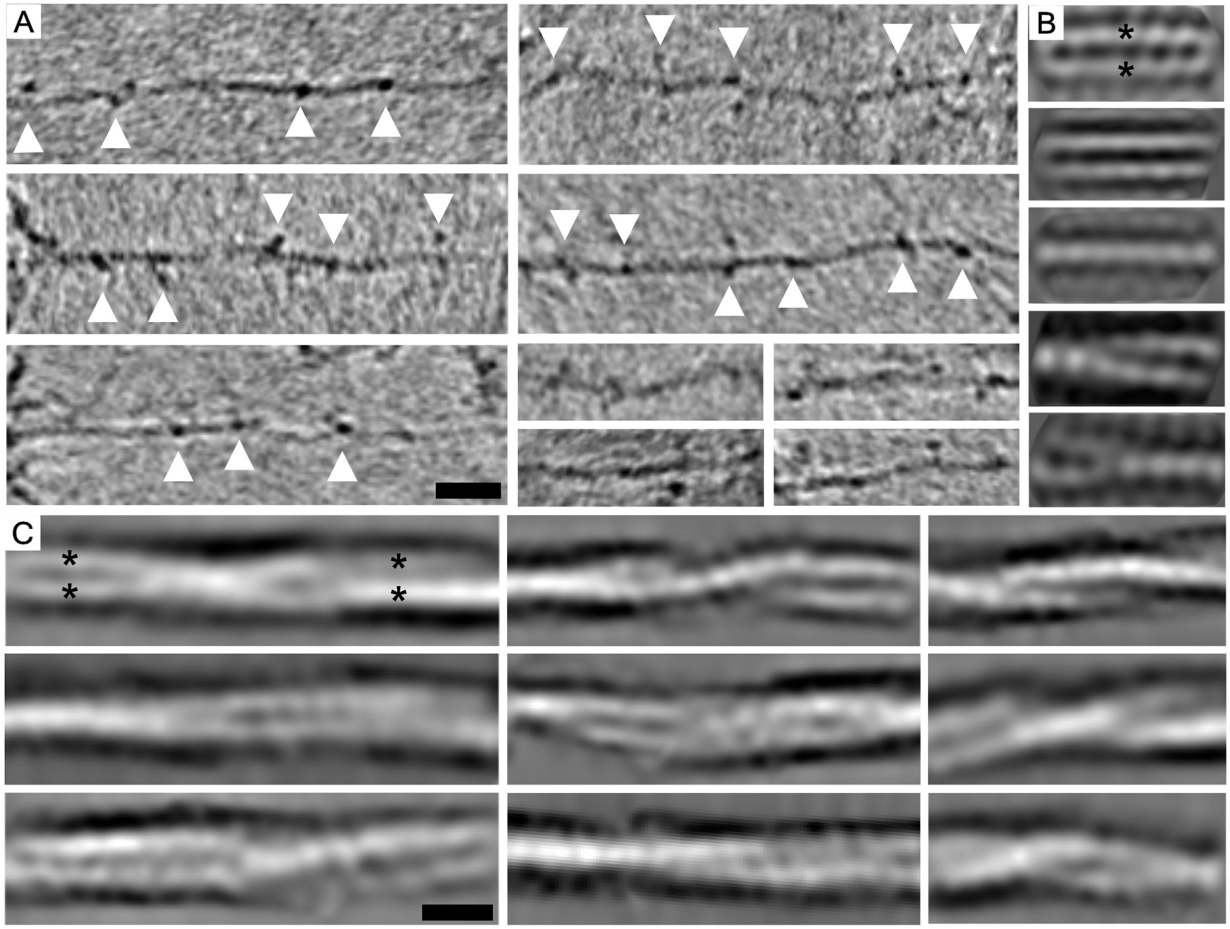

Fig. 4. Structural analysis of lamin filaments in ghost nuclei from *Lmna*$^{H222P/H222P}$ MEFs. (A) A set of individual filaments at the nuclear envelope from a cryo-tomogram of an *Lmna*$^{H222P/H222P}$ MEF ghost nucleus. The filaments are mostly curved and structurally heterogeneous. Globular structures along the lamin filaments (arrowheads) are presumably the Ig-like domains, which exhibit variability in position. Scale bar: 20 nm. (B) Individual two-dimensional class averages, 12 nm long, show different views into lamin filament organization and orientations. All class averages are shown in Fig. S5B. Asterisks in the top panel indicate the two filamentous substructures, which are shown in the other panels interacting with each other, crossing over each other and even being situated one behind the other (middle panel). (C) Reconstituted filaments show detailed organization of the filaments and their substructures. The 2D averaged classes (as shown in B) were used to map back the averaged structures to form reconstituted filaments with the correct order. Asterisks indicate protofilaments interacting and crossing each other. Scale bar: 4 nm (B,C).

composed of both A- and B-type lamins, although in *Lmna*$^{H222P/H222P}$ fibroblasts, we found that B-type lamin expression was upregulated relative to that in wild-type fibroblasts. We analyzed a large number of lamin filaments – more than 950,000 filament segments from 233 tomograms – ensuring, with a high statistical confidence, the close structural resemblance of lamin A/C H222P filaments to wild-type filaments. The H222P amino acid substitution in lamin A/C is situated in a linker domain, between coil 1 and 2; therefore, this region presumably can accommodate the mutation without a major structural alteration.

The assembly of lamin dimers into polymers is central for understanding the basic characteristics of the filaments. A recent publication suggested that lamins interact laterally through coil 1 and 2 to form a tetrameric structure (Ahn et al., 2019). This is similar to cytoplasmic IFs (Herrmann and Aebi, 2004). Our experiments revealed the existence of two protofilaments ∼1.8 nm in thickness, which have the dimensions of a dimeric coiled-coil structure (Zaccai et al., 2011). This observation supports the notion that two head-to-tail filaments are the basic lamin components that interact to form the mature filaments (Stuurman et al., 1998). Moreover, our *in silico* reconstituted filaments provide evidence that the interactions between the two head-to-tail polymers of dimers are not structurally homogeneous (Figs 4 and 5, arrowheads), allowing lamin filaments to adopt a spectrum of conformations that are presumably crucial to their flexibility and the required changes upon the introduction of external forces (Cho et al., 2019; Maurer and Lammerding, 2019; Sapra et al., 2020).

Pathogenic *LMNA* mutations leading to many different amino acid substitutions along the lamin A/C proteins cause striated muscle disease (Briand et al., 2018; Cattin et al., 2013; Maggi et al., 2016; Perrot et al., 2009; Tatli and Medalia, 2018). These mutations appear to result in a loss of some aspect of lamin A/C function, as human patients with *LMNA* mutations leading to haploinsufficiency and *Lmna*-null mice both develop striated muscle disease (Bonne et al., 1999; Sullivan et al., 1999). However, how these lamin A/C amino acid substitutions cause cardiomyopathy and muscular dystrophy is poorly understood. Among several hypotheses, it is proposed that the pathogenic lamin A/C variants lead to altered chromatin organization, gene expression and cellular mechanotransduction (Osmanagic-Myers and Foisner, 2019; Schreiber and Kennedy, 2013). Our results provide structural insights into how a striated muscle disease-causing lamin A/C variant affects nuclear structure. In *Lmna*$^{H222P/H222P}$

Journal of Cell Science (2021) 134, jcs256156. doi:10.1242/jcs.256156

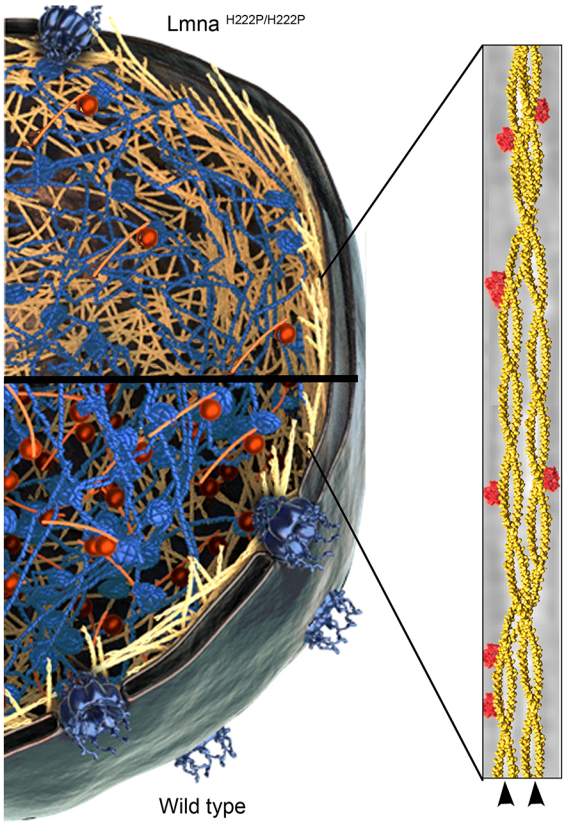

Fig. 5. Nuclear envelope and lamins in wild-type and *Lmna*$^{H222P/H222P}$ MEFs. Left: model showing the nuclear lamina (yellow) of wild-type MEFs (bottom), which has tight interactions with chromatin (blue) and chromatin-binding factors (red). In *Lmna*$^{H222P/H222P}$ MEFs (top), the nuclear lamin filaments are more exposed. Right: the structure of the lamin filaments composed of two head-to-tail lamin dimeric polymers (arrowheads), which interact to form a variety of structures. The model is superimposed on an image of reconstituted filaments (Fig. 4), with the Ig-like fold domains (red) added subjectively to resemble their appearance in Fig. 4A.

MEFs, the overall organization of lamins in the nuclear lamina appears unaffected by the amino acid substitution. However, nuclei are slightly larger with alterations at the lamina–chromatin interface. How these alterations affect the mechanical properties of the nucleus, signaling cascades or gene expression remains to be determined. The normal lamina structure at the resolution of cryo-ET also cannot explain the alterations in nuclear structure observed at the light microscope level in fibroblasts of human subjects with striated muscle disease-causing *LMNA* mutations and in transfected cultured cells expressing the pathogenic lamin A variants (Muchir et al., 2004; Ostlund et al., 2001; Raharjo et al., 2001).

Using cryo-ET to examine additional cells expressing different lamin A/C variants could lead to a better understanding of the structure of nuclear lamins and filament assembly. Combining these studies with *in vitro* assembly assays of lamin filaments will lead to a higher-resolution structure of lamins and understanding of lamina assembly. Examination of cells from mice and human subjects with other mutations that cause striated muscle disease and other laminopathies, such as partial lipodystrophy, peripheral neuropathy or progeria, could also provide further insights into pathogenic mechanisms. Furthermore, muscular dystrophy and cardiomyopathy caused by *LMNA* mutations in humans is autosomal dominant. Therefore, the lamin A/C filaments or dimers in the cells of human patients could be composed of both wild-type and variant proteins. The autosomal-dominant nature of most human laminopathies would therefore provide an additional challenge in scrutinizing the effects of the disease-causing variants on lamina structure and pathogenic mechanisms.

MATERIALS AND METHODS

Preparation and immortalization of MEFs

MEFs were isolated from embryos at embryonic day 14–15 (E14–E15) generated by crosses between *Lmna*$^{H222P/+}$ male and female mice. Briefly, each embryo was cut into fine pieces and incubated at 37°C for 15 min in 1 ml 0.25% trypsin (Gibco, 25200-056). The tissue pieces were then sheared in an 18 gauge needle attached to a syringe, and trypsin was inactivated by addition of DMEM supplemented with high glucose, sodium pyruvate, GlutaMAX and Phenol Red (Gibco, 10569-010) and containing 15% (v/v) fetal bovine serum (Gibco, 26140-079). Cells were then plated in 10 cm culture dishes and allowed to adhere for 24 h. Non–adherent cells were discarded, and the adherent fraction were the MEFs. To establish the immortalized lines, MEFs at passage 2 were infected with a packaged retrovirus that expresses SV40 large T antigen (a gift from Drs Eros Lazzerini Denchi and Larry Gerace, The Scripps Research Institute, USA). Stable immortalized MEF pools were established by selecting the infected cells in 400 µg/ml geneticin (Gibco, 10131035). Genotypes of the embryos and MEFs were confirmed by PCR as previously described (Arimura et al., 2005). The Institutional Animal Care and Use Committee at Columbia University Irving Medical Center approved the protocol.

Cell culture

Immortalized wild-type and *Lmna*$^{H222P/H222P}$ MEFs were cultured in DMEM (Sigma-Aldrich, D5671) supplemented with 10% (v/v) FCS (Sigma-Aldrich, F7524), 1% penicillin-streptomycin (Sigma-Aldrich, P0781), 2 mM L-glutamine (Sigma-Aldrich, G7513), and 400 µg/ml geneticin at 37°C and 5% CO_2 in a humidified incubator. Confluent cells were trypsinized (Sigma-Aldrich, T4174) and seeded onto glow-discharged holey-carbon-covered EM grids (R 2/1, Au 200, Quantifoil). After ∼16 h, the grids were subjected to nuclease treatment or they were directly plunge frozen in liquid nitrogen-cooled ethane for FIB milling.

Knockdown of vimentin in MEFs

Transfection using the committal vimentin shRNA lentiviral vector (Sigma-Aldrich) and the PolyPlus protocol (Jetprime) yielded 60–80% vimentin knockdown. At 24 h post transfection, the medium was replaced with DMEM supplement with high glucose, 2 mM L-glutamine, 1% penicillin-streptomycin, 15% (v/v) FCS, 1% sodium pyruvate, 400 µg/ml geneticin and 4 µg/ml puromycin. All untransfected cells died upon the addition of this medium. The transfected cells were expanded and analyzed by immunoblotting.

Quantitative immunofluorescence microscopy

MEFs were seeded onto glass coverslips coated with fibrinogen (50 µg/ml; Sigma-Aldrich, 341576) for 3.5 h in 10% (v/v) FCS. Cells were synchronized by serum starvation for 16 h in 1% FCS. Cells were then fixed in 4% (w/v) paraformaldehyde (Sigma-Aldrich, 16005) for 10 min before being permeabilized in 0.1% Triton X-100 (Sigma-Aldrich, T8787) for 10 min. Permeabilized cells were incubated in a blocking buffer [2% (w/v) BSA, 22.5 mg/ml glycine in PBS with 0.1% Tween-20; PBST] for 1 h at 25°C. The cells were incubated in the respective primary antibodies, diluted in blocking buffer, for 1 h at 25°C. The following primary antibodies were used: anti-lamin A/C (Santa Cruz, sc-376248; 1:100), anti-lamin B1 (Santa Cruz, sc-6217; 1:200), anti-H3K9me3 (Abcam, ab8898; 1:700) and anti-H3K27ac (Abcam, ab4729; 1:350). After 3×5 min washes in PBST, the cells were incubated with the secondary antibodies, diluted in blocking buffer for 1 h at 25°C. The following secondary antibodies were used: Alexa Fluor 488-conjugated donkey anti-goat IgG (Jackson ImmunoResearch 705-545-003; 1:400), Cy3-conjugated donkey anti-rabbit IgG (Jackson ImmunoResearch 711-165-152; 1:400) and Cy3-conjugated donkey anti-mouse IgG (Jackson ImmunoResearch 715-165-150; 1:400). Immunostained cells were washed 3× for 5 min in PBST and 3× for 5 min in PBS before being incubated with

Journal of Cell Science (2021) 134, jcs256156. doi:10.1242/jcs.256156

Hoechst 33342 (Sigma-Aldrich, B2261) for 15 min at 25°C. After three final washes for 5 min each in PBS, the coverslips were mounted on glass slides with Dako mounting medium (Agilent, S3023) and sealed with nail polish.

Cells were analyzed using an automated inverted microscope (Leica Microsystems, DMI4000 B) equipped with a fluorescence lamp (Leica Microsystems, EL6000), A4/GFP/RFP filters and a monochromatic digital camera (Leica Microsystems, DFC365 FX). Images for quantitative analysis were acquired with a 20× air objective (Leica Microsystems, HCX PL Floutar 20×/0.4). Image analysis was conducted using ImageJ (Schneider et al., 2012). Thresholding of the image was applied manually in the Hoechst channel. Next, the image was used to define the nuclei, their area and the average signal intensity of each channel obtained using the 'Analyze Particles' function. The measured signal intensities for each channel were normalized to the median of the corresponding wild-type intensity and the measured area of the nucleus. For TIRF microscopy, the slides were prepared as described above. TIRF microscopy was performed on an inverted widefield microscope (Leica Microsystems, DMI6000B) equipped with an Andor iXon Ultra 897 EMCCD camera and a LQ-HXP 120 illumination source. TIRF images were acquired using a 160× oil objective (Leica Microsystems, HC PL APO 160×/1.43 OIL) and with a penetration depth of 90 nm, using 488T and 532HP-T filters.

To analyze nuclear surface area and volume, we acquired 3D confocal stacks of nuclei stained for lamin A/C (Leica SP8 FALCON automated inverted confocal laser scanning microscope, equipped with HyD SMD detectors, Leica Microsystems). Stacks were acquired using a HC PL APO corr CS2 63×/1.40 OIL objective (Leica Microsystems). Cy3-conjugated secondary antibody was excited using a white light laser (WLL) at 553 nm. Emission was detected with a HyD SMD detector set to 568–620 nm. Stacks were analyzed using Imaris 9.6.0. (Oxford Instruments).

Immunoblotting

For immunoblotting, MEFs were lysed in 1× cell lysis buffer (Cell Signaling Technology, 9803) with proteinase inhibitor cocktail (Sigma-Aldrich, P8340) and 1 mM PMSF (Sigma-Aldrich, 93482-50ML-F). Proteins in the cell lysates were separated by SDS–PAGE. Immunoblots were performed using anti-lamin B1 (Cance et al., 1992; 1:1000), anti-lamin B2 (Invitrogen, 33-2100; 1:500), anti-H3K9me3 (Abcam, ab8898; 1:1000), anti-Lamin A/C (Santa Cruz, SC-20681; 1:5000), anti-γ-tubulin (Sigma-Aldrich, T-5326; 1:1000) and anti-GAPDH (Ambion, AM4300; 1:5000) antibodies. Quantification of blots was performed using ImageJ, with normalization to loading controls as indicated, and presented as fold change over untreated or wild-type MEFs.

Preparation of ghost nuclei on EM grids

Cells growing on EM grids were rinsed in PBS supplemented with 2 mM $MgCl_2$, permeabilized for 15–20 s in a permeabilization buffer (1× PBS, 0.1% Triton X-100, 600 mM KCl, 10 mM $MgCl_2$ and protease inhibitors; Roche, 37378900) and rinsed again. Thereafter, grids were treated with 2.5 units/µl benzonase (Merck, 71206-3) in PBS containing 2 mM $MgCl_2$ for 30 min, washed again prior to applying 3 µl of fiducial gold markers (Aurion; 10 nm, BSA-coated) and then plunge frozen in liquid ethane.

Cryo-FIB-scanning electron microscopy milling

Prior to FIB milling, the grids were coated with 5 nm Pt/C using a Leica BAF060 system cooled to −160° C. The grids were transferred to a Zeiss Auriga 40 Crossbeam FIB-SEM. Using the gas injection system, an organometallic platinum protective layer was applied to the grids. Cells were milled with a focused gallium ion beam at a stage temperature of less than −150°C and a stage angle of 18°. The milling was controlled by the NanoPatterning and Visualization Engine software (Zeiss) and observed by scanning electron microscopy. Final thickness of FIB-milled lamellas were 100–200 nm.

Cryo-ET acquisition

Tilt series were acquired of FIB-milled lamellas and ghost nuclei using a Titan Krios electron microscope (operated at 300 keV) equipped with a Gatan Quantum Energy Filter and a K2 Summit direct electron detection camera. All tilt series were acquired at a magnification of 64,000× and 4–6 µm underfocus using SerialEM (Mastronarde, 2005), resulting in a 0.22 nm/pixel at the specimen level. The data covered an angular range of −60° to 60°, acquired from −30° to 60° followed by −30° to −60°, every 2°, with a total dose of 100–140 $e^-/Å^2$. Tilt series acquisition for FIB-milled lamellas were conducted by a dose symmetric tilt scheme (Hagen et al., 2017) from −60° to 60° every 3° with a total dose of 150 $e^-/Å^2$. A total of 45 tilt series were acquired from FIB-milled lamellae, and 233 tilt series were acquired for ghost nuclei.

Immunogold labeling of lamin A/C

Immunogold labeling was performed as previously described (Turgay et al., 2017). In brief, MEFs grown on EM grids were permeabilized, nuclease treated as described above and fixed in 4% paraformaldehyde. After incubation with anti-lamin A/C antibody (Abcam, ab133256; 1:150) and washing, the cells were incubated with 6-nm gold particles coupled to protein A (Aurion). Controls for unspecific binding were performed without the addition of the antibody. After the final washing steps, the grids were plunge frozen with addition of 10-nm gold particles (Aurion) for alignment and then stored in liquid nitrogen. Images for quantitative analysis of 6-nm gold particle distribution were acquired at a magnification of 42,000×, with a pixel size of 3.4 Å (0.34 nm). Gold particles were classified and counted using ImageJ.

Cryo-ET image processing

All tilt series were reconstructed by using the IMOD workflow (Mastronarde and Held, 2017). For visualization purposes, the tomographic slices picked for the visualization were reconstructed using the SIRT algorithm, and eight *z* slices were projected in the slicer window in IMOD. A dataset of tomograms with −4 µm defocus and 120 e^-/A^2 were selected for image averaging. The tomograms were reconstructed again in MATLAB using the TOM Toolbox (Nickell et al., 2005). Thereafter, the APT workflow (Martins et al., 2021) was followed. Ten manually segmented tomograms (Amira-Avizo 2019.1, Thermo Fisher Scientific) were used as a reference for the neural network segmentation with EMAN 2.3 (Tang et al., 2007). Evenly spaced coordinates every 5 nm along the filaments were picked to determine the centre of each segment along the filament axis. Approximately 967,000 sub-volumes ($12×12×4.4\ nm^3$) were reconstructed around the picked coordinates and projected to 2D images. The projected images were imported into Relion 3.0 (Zivanov et al., 2018). After several rounds of classifications, 200 class averages with a total number of 350,000 particles were obtained. The final 2D class averages were mapped-back two or more sequential segments along a filament and were selected and mapped back to their *x*–*y* positions. Surface rendering images of wild-type and $Lmna^{H222P/H222P}$ MEF tomograms were generated using the Amira-Avizo 2019.1 software package. Segmentation of nucleosomes and ribosomes in the FIB data was performed automatically in EMAN 2.3 (Tang et al., 2007) with a neural network. False positives were removed manually.

Acknowledgements

We thank the Center for Microscopy and Image Analysis at the University of Zurich (ZMB), Dr Yagmur Turgay for technical help in the initial stages, and Drs Eros Lazzerini Denchi and Larry Gerace for reagents and advice on immortalizing MEFs.

Competing interests

The authors declare no competing or financial interests.

Author contributions

Conceptualization: O.M.; Methodology: O.M., M.E., H.J.W.; Software: M.T., M.E.; Validation: M.T., M.E., W.W., J.-Y.S., H.J.W.; Formal analysis: R.K.-T., M.T.; Investigation: R.K.-T., M.T., W.W., J.-Y.S.; Resources: M.E., G.B.; Writing - original draft: O.M., H.J.W.; Writing - review & editing: R.K.-T., M.T., M.E., W.W., J.-Y.S., G.B., H.J.W.; Visualization: R.K.-T., M.T.; Supervision: O.M., M.E., H.J.W.; Project administration: O.M.; Funding acquisition: O.M.

Funding

This work was funded by grants from the Schweizerischer Nationalfonds zur Förderung der Wissenschaftlichen Forschung (SNSF 31003A_179418) and the Mäxi Foundation to O.M. and by a grant from the U.S. National Institutes of Health (R01AR04897) to H.J.W. Deposited in PMC for release after 12 months.

Data availability

Representative cryo-electron tomography data have been deposited in the Electron Microscopy Data Bank under accession code EMPAIR-10601.

Supplementary information

Supplementary information available online at
https://jcs.biologists.org/lookup/doi/10.1242/jcs.256156.supplemental

Peer review history

The peer review history is available online at
https://jcs.biologists.org/lookup/doi/10.1242/jcs.256156.reviewer-comments.pdf

References

Ahn, J., Jo, I., Kang, S.-M., Hong, S., Kim, S., Jeong, S., Kim, Y.-H., Park, B.-J. and Ha, N.-C. (2019). Structural basis for lamin assembly at the molecular level. *Nat. Commun.* **10**, 3757. doi:10.1038/s41467-019-11684-x

Arimura, T., Helbling-Leclerc, A., Massart, C., Varnous, S., Niel, F., Lacène, E., Fromes, Y., Toussaint, M., Mura, A.-M., Keller, D. I. et al. (2005). Mouse model carrying H222P-Lmna mutation develops muscular dystrophy and dilated cardiomyopathy similar to human striated muscle laminopathies. *Hum. Mol. Genet.* **14**, 155-169. doi:10.1093/hmg/ddi017

Bertrand, A. T., Brull, A., Azibani, F., Benarroch, L., Chikhaoui, K., Stewart, C. L., Medalia, O., Ben Yaou, R. and Bonne, G. (2020). Lamin A/C assembly defects in LMNA-congenital muscular dystrophy is responsible for the increased severity of the disease compared with emery-dreifuss muscular dystrophy. *Cells* **9**, 844. doi:10.3390/cells9040844

Bonne, G., Di Barletta, M. R., Varnous, S., Bécane, H.-M., Hammouda, E.-H., Merlini, L., Muntoni, F., Greenberg, C. R., Gary, F., Urtizberea, J. A. et al. (1999). Mutations in the gene encoding lamin A/C cause autosomal dominant Emery-Dreifuss muscular dystrophy. *Nat. Genet.* **21**, 285-288. doi:10.1038/6799

Bonne, G., Mercuri, E., Muchir, A., Urtizberea, A., Becane, H. M., Recan, D., Merlini, L., Wehnert, M., Boor, R., Reuner, U. et al. (2000). Clinical and molecular genetic spectrum of autosomal dominant Emery-Dreifuss muscular dystrophy due to mutations of the lamin A/C gene. *Ann. Neurol.* **48**, 170-180. doi:10.1002/1531-8249(200008)48:2<170::AID-ANA6>3.0.CO;2-J

Briand, N., Guénantin, A.-C., Jeziorowska, D., Shah, A., Mantecon, M., Capel, E., Garcia, M., Oldenburg, A., Paulsen, J., Hulot, J.-S. et al. (2018). The lipodystrophic hotspot lamin A p.R482W mutation deregulates the mesodermal inducer T/Brachyury and early vascular differentiation gene networks. *Hum. Mol. Genet.* **27**, 1447-1459. doi:10.1093/hmg/ddy055

Cance, W. G., Chaudhary, N., Worman, H. J., Blobel, G. and Cordoncardo, C. (1992). Expression of the nuclear lamins in normal and neoplastic human tissues. *J. Exp. Clin. Cancer Res.* **11**, 233-246.

Cattin, M.-E., Muchir, A. and Bonne, G. (2013). 'State-of-the-heart' of cardiac laminopathies. *Curr. Opin. Cardiol.* **28**, 297-304. doi:10.1097/HCO.0b013e32835f0c79

Chatzifrangkeskou, M., Kah, D., Lange, J. R., Goldmann, W. H. and Muchir, A. (2020). Mutated lamin A modulates stiffness in muscle cells. *Biochem. Biophys. Res. Commun.* **529**, 861-867. doi:10.1016/j.bbrc.2020.05.102

Cho, S., Vashisth, M., Abbas, A., Majkut, S., Vogel, K., Xia, Y., Ivanovska, I. L., Irianto, J., Tewari, M., Zhu, K. et al. (2019). Mechanosensing by the lamina protects against nuclear rupture, DNA damage, and cell-cycle arrest. *Dev. Cell* **49**, 920-935.e5. doi:10.1016/j.devcel.2019.04.020

Choi, J. C., Wu, W., Phillips, E., Plevin, R., Sera, F., Homma, S. and Worman, H. J. (2018). Elevated dual specificity protein phosphatase 4 in cardiomyopathy caused by lamin A/C gene mutation is primarily ERK1/2-dependent and its depletion improves cardiac function and survival. *Hum. Mol. Genet.* **27**, 2290-2305. doi:10.1093/hmg/ddy134

Constantinescu, D., Gray, H. L., Sammak, P. J., Schatten, G. P. and Csoka, A. B. (2006). Lamin A/C expression is a marker of mouse and human embryonic stem cell differentiation. *Stem Cells* **24**, 177-185. doi:10.1634/stemcells.2004-0159

de Leeuw, R., Gruenbaum, Y. and Medalia, O. (2018). Nuclear Lamins: thin Filaments with Major Functions. *Trends Cell Biol.* **28**, 34-45. doi:10.1016/j.tcb.2017.08.004

Dhe-Paganon, S., Werner, E. D., Chi, Y.-I. and Shoelson, S. E. (2002). Structure of the globular tail of nuclear lamin. *J. Biol. Chem.* **277**, 17381-17384. doi:10.1074/jbc.C200038200

Fisher, D. Z., Chaudhary, N. and Blobel, G. (1986). cDNA sequencing of nuclear lamins A and C reveals primary and secondary structural homology to intermediate filament proteins. *Proc. Natl. Acad. Sci. USA* **83**, 6450-6454. doi:10.1073/pnas.83.17.6450

Goldman, R. D., Shumaker, D. K., Erdos, M. R., Eriksson, M., Goldman, A. E., Gordon, L. B., Gruenbaum, Y., Khuon, S., Mendez, M., Varga, R. et al. (2004). Accumulation of mutant lamin A causes progressive changes in nuclear architecture in Hutchinson-Gilford progeria syndrome. *Proc. Natl. Acad. Sci. USA* **101**, 8963-8968. doi:10.1073/pnas.0402943101

Gruenbaum, Y. and Foisner, R. (2015). Lamins: nuclear intermediate filament proteins with fundamental functions in nuclear mechanics and genome regulation. *Annu. Rev. Biochem.* **84**, 131-164. doi:10.1146/annurev-biochem-060614-034115

Hagen, W. J. H., Wan, W. and Briggs, J. A. G. (2017). Implementation of a cryo-electron tomography tilt-scheme optimized for high resolution subtomogram averaging. *J. Struct. Biol.* **197**, 191-198. doi:10.1016/j.jsb.2016.06.007

Harapin, J., Börmel, M., Sapra, K. T., Brunner, D., Kaech, A. and Medalia, O. (2015). Structural analysis of multicellular organisms with cryo-electron tomography. *Nat. Methods* **12**, 634-636. doi:10.1038/nmeth.3401

Herrmann, H. and Aebi, U. (2004). Intermediate filaments: molecular structure, assembly mechanism, and integration into functionally distinct intracellular Scaffolds. *Annu. Rev. Biochem.* **73**, 749-789. doi:10.1146/annurev.biochem.73.011303.073823

Kapinos, L. E., Burkhard, P., Herrmann, H., Aebi, U. and Strelkov, S. V. (2011). Simultaneous formation of right- and left-handed anti-parallel coiled-coil interfaces by a coil2 fragment of human lamin A. *J. Mol. Biol.* **408**, 135-146. doi:10.1016/j.jmb.2011.02.037

Kim, Y., Sharov, A. A., McDole, K., Cheng, M., Hao, H., Fan, C.-M., Gaiano, N., Ko, M. S. H. and Zheng, Y. (2011). Mouse B-type lamins are required for proper organogenesis but not by embryonic stem cells. *Science* **334**, 1706-1710. doi:10.1126/science.1211222

Klapper, M., Exner, K., Kempf, A., Gehrig, C., Stuurman, N., Fisher, P. A. and Krohne, G. (1997). Assembly of A- and B-type lamins studied in vivo with the baculovirus system. *J. Cell Sci.* **110**, 2519-2532.

Krimm, I., Östlund, C., Gilquin, B., Couprie, J., Hossenlopp, P., Mornon, J.-P., Bonne, G., Courvalin, J.-C., Worman, H. J. and Zinn-Justin, S. (2002). The Ig-like structure of the C-terminal domain of lamin A/C, mutated in muscular dystrophies, cardiomyopathy, and partial lipodystrophy. *Structure* **10**, 811-823. doi:10.1016/S0969-2126(02)00777-3

Lilina, A. V., Chernyatina, A. A., Guzenko, D. and Strelkov, S. V. (2019). Lateral A11 type tetramerization in lamins. *J. Struct. Biol.* **209**, 107404. doi:10.1016/j.jsb.2019.10.006

Maggi, L., Carboni, N. and Bernasconi, P. (2016). Skeletal muscle laminopathies: a review of clinical and molecular features. *Cells* **5**, 33. doi:10.3390/cells5030033

Makarov, A. A., Zou, J., Houston, D. R., Spanos, C., Solovyova, A. S., Cardenal-Peralta, C., Rappsilber, J. and Schirmer, E. C. (2019). Lamin A molecular compression and sliding as mechanisms behind nucleoskeleton elasticity. *Nat. Commun.* **10**, 3056. doi:10.1038/s41467-019-11063-6

Martins, B., Sorrentino, S., Chung, W.-L., Tatli, M., Medalia, O. and Eibauer, M. (2021). Unveiling the polarity of actin filaments by cryo-electron tomography. *Structure* **11**, S0969-2126(20)30481-0. doi:10.1016/j.str.2020.12.014

Mastronarde, D. N. (2005). Automated electron microscope tomography using robust prediction of specimen movements. *J. Struct. Biol.* **152**, 36-51. doi:10.1016/j.jsb.2005.07.007

Mastronarde, D. N. and Held, S R. (2017). Automated tilt series alignment and tomographic reconstruction in IMOD. *J Struct Biol.* **197**, 102-113. doi:10.1016/j.jsb.2016.07.011

Maurer, M. and Lammerding, J. (2019). The driving force: nuclear mechanotransduction in cellular function, fate, and disease. *Annu. Rev. Biomed. Eng.* **21**, 443-468. doi:10.1146/annurev-bioeng-060418-052139

McKeon, F. D., Kirschner, M. W. and Caput, D. (1986). Homologies in both primary and secondary structure between nuclear envelope and intermediate filament proteins. *Nature* **319**, 463-468. doi:10.1038/319463a0

Muchir, A., Medioni, J., Laluc, M., Massart, C., Arimura, T., van der Kooi, A. J., Desguerre, I., Mayer, M., Ferrer, X., Briault, S. et al. (2004). Nuclear envelope alterations in fibroblasts from patients with muscular dystrophy, cardiomyopathy, and partial lipodystrophy carrying lamin A/C gene mutations. *Muscle Nerve* **30**, 444-450. doi:10.1002/mus.20122

Muchir, A., Reilly, S. A., Wu, W., Iwata, S., Homma, S., Bonne, G. and Worman, H. J. (2012). Treatment with selumetinib preserves cardiac function and improves survival in cardiomyopathy caused by mutation in the lamin A/C gene. *Cardiovasc. Res.* **93**, 311-319. doi:10.1093/cvr/cvr301

Naetar, N., Ferraioli, S. and Foisner, R. (2017). Lamins in the nuclear interior - life outside the lamina. *J. Cell Sci.* **130**, 2087-2096. doi:10.1242/jcs.203430

Nickell, S., Förster, F., Linaroudis, A., Net, W. D., Beck, F., Hegerl, R., Baumeister, W. and Plitzko, J. M. (2005). TOM software toolbox: acquisition and analysis for electron tomography. *J. Struct. Biol.* **149**, 227-34. doi:10.1016/j.jsb.2004.10.006

Nicolas, H. A., Akimenko, M.-A. and Tesson, F. (2019). Cellular and animal models of striated muscle laminopathies. *Cells* **8**, 291. doi:10.3390/cells8040291

Osmanagic-Myers, S. and Foisner, R. (2019). The structural and gene expression hypotheses in laminopathic diseases-not so different after all. *Mol. Biol. Cell* **30**, 1786-1790. doi:10.1091/mbc.E18-10-0672

Ostlund, C., Bonne, G., Schwartz, K. and Worman, H. J. (2001). Properties of lamin A mutants found in Emery-Dreifuss muscular dystrophy, cardiomyopathy and Dunnigan-type partial lipodystrophy. *J. Cell Sci.* **114**, 4435-4445.

Perrot, A., Hussein, S., Ruppert, V., Schmidt, H. H. J., Wehnert, M. S., Duong, N. T., Posch, M. G., Panek, A., Dietz, R., Kindermann, I. et al. (2009). Identification of mutational hot spots in LMNA encoding lamin A/C in patients with familial dilated cardiomyopathy. *Basic Res. Cardiol.* **104**, 90-99. doi:10.1007/s00395-008-0748-6

Pfeifer, C. R., Irianto, J. and Discher, D. E. (2019). Nuclear mechanics and cancer cell migration. *Adv. Exp. Med. Biol.* **1146**, 117-130. doi:10.1007/978-3-030-17593-1_8

Raharjo, W. H., Enarson, P., Sullivan, T., Stewart, C. L. and Burke, B. (2001). Nuclear envelope defects associated with LMNA mutations cause dilated cardiomyopathy and Emery-Dreifuss muscular dystrophy. *J. Cell Sci.* **114**, 4447-4457.

Rigort, A., Bauerlein, F. J. B., Villa, E., Eibauer, M., Laugks, T., Baumeister, W. and Plitzko, J. M. (2012). Focused ion beam micromachining of eukaryotic cells for cryoelectron tomography. *Proc. Natl. Acad. Sci. USA* **109**, 4449-4454. doi:10.1073/pnas.1201333109

Sapra, K. T., Qin, Z., Dubrovsky-Gaupp, A., Aebi, U., Müller, D. J., Buehler, M. J. and Medalia, O. (2020). Nonlinear mechanics of lamin filaments and the meshwork topology build an emergent nuclear lamina. *Nat. Commun.* **11**, 6205. doi:10.1038/s41467-020-20049-8

Scaffidi, P. and Misteli, T. (2008). Lamin A-dependent misregulation of adult stem cells associated with accelerated ageing. *Nat. Cell Biol.* **10**, 452-459. doi:10.1038/ncb1708

Schneider, C. A., Rasband, W. S. and Eliceiri, K. W. (2012). NIH Image to ImageJ: 25 years of image analysis. *Nat. Methods* **9**, 671-675. doi:10.1038/nmeth.2089

Schreiber, K. H. and Kennedy, B. K. (2013). When lamins go bad: nuclear structure and disease. *Cell* **152**, 1365-1375. doi:10.1016/j.cell.2013.02.015

Steinert, P. M. and Roop, D. R. (1988). Molecular and cellular biology of intermediate filaments. *Annu. Rev. Biochem.* **57**, 593-625. doi:10.1146/annurev.bi.57.070188.003113

Strelkov, S. V., Schumacher, J., Burkhard, P., Aebi, U. and Herrmann, H. (2004). Crystal structure of the human lamin A coil 2B dimer: implications for the head-to-tail association of nuclear lamins. *J. Mol. Biol.* **343**, 1067-1080. doi:10.1016/j.jmb.2004.08.093

Stuurman, N., Heins, S. and Aebi, U. (1998). Nuclear lamins: their structure, assembly, and interactions. *J. Struct. Biol.* **122**, 42-66. doi:10.1006/jsbi.1998.3987

Sullivan, T., Escalante-Alcalde, D., Bhatt, H., Anver, M., Bhat, N., Nagashima, K., Stewart, C. L. and Burke, B. (1999). Loss of A-type lamin expression compromises nuclear envelope integrity leading to muscular dystrophy. *J. Cell Biol.* **147**, 913-920. doi:10.1083/jcb.147.5.913

Tang, G., Peng, L., Baldwin, P. R., Mann, D. S., Jiang, W., Rees, I. and Ludtke, S. J. (2007). EMAN2: an extensible image processing suite for electron microscopy. *J. Struct. Biol.* **157**, 38-46. doi:10.1016/j.jsb.2006.05.009

Tatli, M. and Medalia, O. (2018). Insight into the functional organization of nuclear lamins in health and disease. *Curr. Opin. Cell Biol.* **54**, 72-79. doi:10.1016/j.ceb.2018.05.001

Tenga, R. and Medalia, O. (2020). Structure and unique mechanical aspects of nuclear lamin filaments. *Curr. Opin. Struct. Biol.* **64**, 152-159. doi:10.1016/j.sbi.2020.06.017

Turgay, Y. and Medalia, O. (2017). The structure of lamin filaments in somatic cells as revealed by cryo-electron tomography. *Nucleus* **8**, 475-481. doi:10.1080/19491034.2017.1337622

Turgay, Y., Eibauer, M., Goldman, A. E., Shimi, T., Khayat, M., Ben-Harush, K., Dubrovsky-Gaupp, A., Sapra, K. T., Goldman, R. D. and Medalia, O. (2017). The molecular architecture of lamins in somatic cells. *Nature* **543**, 261-264. doi:10.1038/nature21382

Vigouroux, C., Auclair, M., Dubosclard, E., Pouchelet, M., Capeau, J., Courvalin, J. C. and Buendia, B. (2001). Nuclear envelope disorganization in fibroblasts from lipodystrophic patients with heterozygous R482Q/W mutations in the lamin A/C gene. *J. Cell Sci.* **114**, 4459-4468.

Weber, M. S., Wojtynek, M. and Medalia, O. (2019). Cellular and structural studies of eukaryotic cells by cryo-electron tomography. *Cells* **8**, 57. doi:10.3390/cells8010057

Worman, H. J. (2012). Nuclear lamins and laminopathies. *J. Pathol.* **226**, 316-325. doi:10.1002/path.2999

Worman, H. J. and Bonne, G. (2007). "Laminopathies": a wide spectrum of human diseases. *Exp. Cell Res.* **313**, 2121-2133. doi:10.1016/j.yexcr.2007.03.028

Zaccai, N. R., Chi, B., Thomson, A. R., Boyle, A. L., Bartlett, G. J., Bruning, M., Linden, N., Sessions, R. B., Booth, P. J., Brady, R. L. et al. (2011). A de novo peptide hexamer with a mutable channel. *Nat. Chem. Biol.* **7**, 935-941. doi:10.1038/nchembio.692

Zivanov, J., Nakane, T., Forsberg, B. O., Kimanius, D., Hagen, W. J., Lindahl, E. and Scheres, S. H. (2018). New tools for automated high-resolution cryo-EM structure determination in RELION-3. *Elife* **7**, e42166. doi:10.7554/eLife.42166

Zwerger, M. and Medalia, O. (2013). From lamins to lamina: a structural perspective. *Histochem. Cell Biol.* **140**, 3-12. doi:10.1007/s00418-013-1104-y